Title:

Carbon isotope constraints on the deglacial CO₂ rise from ice cores

Authors:

Jochen Schmitt[1,3*], Robert Schneider[1], Joachim Elsig[1], Daiana Leuenberger[1], Anna Lourantou[2†], Jérôme Chappellaz[2], Peter Köhler[3], Fortunat Joos[1], Thomas F. Stocker[1], Markus Leuenberger[1] & Hubertus Fischer[1,3]

Affiliations:

[1] Climate and Environmental Physics, Physics Institute & Oeschger Centre for Climate Change Research, University of Bern, Switzerland.

[2] UJF – Grenoble 1 / CNRS, Laboratoire de Glaciologie et Géophysique de l'Environnement (LGGE) UMR 5183, Grenoble, France.

[3] Alfred Wegener Institute for Polar and Marine Research, Bremerhaven, Germany.

† Present address: Laboratoire d'Océanographie et du Climat (LOCEAN), Institut Pierre Simon Laplace, Université P. et M. Curie (UPMC), Paris, France.

*Correspondence to: schmitt@climate.unibe.ch

Abstract:

The stable carbon isotope ratio of atmospheric CO_2 ($\delta^{13}C_{atm}$) is a key parameter to decipher past carbon cycle changes. Here we present $\delta^{13}C_{atm}$ data for the last 24,000 years derived from three Antarctic ice cores. We conclude that a pronounced 0.3‰ decrease in $\delta^{13}C_{atm}$ during the early deglaciation can be best explained by upwelling of old, carbon-enriched waters in the Southern Ocean. Later in the deglaciation, regrowth of the terrestrial biosphere, changes in sea surface temperature, and ocean circulation governed the $\delta^{13}C_{atm}$ evolution. During the Last Glacial Maximum, $\delta^{13}C_{atm}$ and CO_2 were essentially constant, suggesting that the carbon cycle was in dynamic equilibrium and that the net transfer of carbon to the deep ocean had occurred before then.

One Sentence Summary:

High-resolution ice core records of stable carbon isotopes in atmospheric CO_2 constrain carbon cycle changes during the Last Glacial Maximum, the early deglacial, and the transition into the Holocene.

Main Text:

During the last 800,000 years (800 kyr), atmospheric CO_2 concentrations have varied in close relation to Antarctic temperatures (*1, 2*) and the general waxing and waning of continental ice sheets. In particular, CO_2 rose from a stable level of 190 parts per million by

46   volume (ppmv) during the Last Glacial Maximum to about 280 ppmv in preindustrial times,

47   showing pronounced differences in atmospheric CO_2 rates of change in the course of the

48   last glacial/interglacial transition (*3*). Many processes have been involved in attempts to

49   explain these CO_2 variations, but it has become evident that none of these mechanisms

50   alone can account for the 90 ppmv increase in atmospheric CO_2. A combination of

51   processes must have been operating (*4, 5*), with their exact timing being crucial. However,

52   a unique solution to the deglacial carbon cycle changes has not been yet found.

53

54   In this respect, high-resolution and precise $\delta^{13}C_{atm}$ records from Antarctic ice cores are

55   needed to better constrain the evolution of carbon cycle changes during the last

56   deglaciation. On millennial time scales, $\delta^{13}C_{atm}$ is primarily influenced by the $\delta^{13}C$ of

57   dissolved inorganic carbon (DIC) ($\delta^{13}C_{DIC}$) and sea surface temperature (SST), which

58   controls the isotopic fractionation during air/sea gas exchange. The continuous rain of

59   isotopically light organic material to the interior of the ocean draws down carbon from the

60   surface layer to intermediate and deep waters, where the organic carbon is remineralized.

61   Consequently, a vertical $\delta^{13}C_{DIC}$ gradient is established, controlled by the interplay of the

62   ocean circulation with this so-called "biological pump". The more intense the circulation,

63   the smaller the gradients are for $\delta^{13}C_{DIC}$, DIC, oxygen and nutrients. Superimposed on these

64   marine carbon cycle processes are climate-induced changes in terrestrial biosphere carbon

65   storage, which result in a net change in the carbon isotopic composition of the

66   ocean/atmosphere system. On orbital time scales, weathering and sedimentation of $CaCO_3$

67   affect $\delta^{13}C_{DIC}$, $\delta^{13}C_{atm}$ and atmospheric CO_2 as well.

68

69   Until recently (*6*), analytical constraints represented the fundamental limitation on the

70   utility of $\delta^{13}C_{atm}$ ice core records (*7, 8*). Here we provide evidence (Fig. 1) about possible

71   causes of carbon cycle changes with measurements of $\delta^{13}C_{atm}$ from two Antarctic ice cores

72   (EPICA (European Project for Ice Coring in Antarctica) Dome C and Talos Dome),

73   performed with three independent methods in two different labs (referred to as Bern

74   sublimation, Bern cracker and Grenoble mill data) (*6, 9*). One of our records is based on a

75   sublimation method (*10*) that avoids the effects associated with incomplete gas extraction

76   and thus yields more precise results (see Supporting Online Material (SOM)). A stringent

77   residual analysis of the three data sets shows virtually no offset between the two Bern data

78   sets and only a small systematic offset between the Bern and Grenoble data of 0.16‰,

79   which can be explained by a method-dependent systematic fractionation. After correction

80   of this offset, we combined the three $\delta^{13}C_{atm}$ records over the last 24 kyr using an error-

81   weighted Monte Carlo bootstrap approach. This method showed that all three data sets are

82   essentially compatible within their analytical uncertainties. To make full use of the

83   resolution and precision of the data, the inclusion of all three data sets is required, although

84   all our conclusions are also supported by the individual records. The final data set consists

85   of 201 individual measurements, each reflecting typically 2 to 4 replicates and with an

86   analytical 1σ error between 0.04 and 0.12‰. Since the resulting Monte Carlo Average

87   (MCA) removes most of the analytical uncertainties, it contains less high-frequency

88   variability compared to the raw data. This is in line with the centennial-scale low-pass

89   filtering inherent to the bubble enclosure process at Dome C. Accordingly, the retained

90 variability can be regarded as the signal most representative of millennial $\delta^{13}C_{atm}$ changes

91 (see SOM for details regarding the MCA and its uncertainty).

92

93 Our $\delta^{13}C_{atm}$ data is in good agreement with previously published lower-resolution records

94 (*6, 9*). Our record shows a very stable level between 24 and ca. 19 kyr before present (BP,

95 where present is defined as 1950), with an average $\delta^{13}C_{atm}$ of -6.45‰ (Tab. S1 and S2),

96 similar to the -6.35‰ of the Late Holocene (Fig. 2B). Given the fact that a large set of

97 environmental parameters such as atmospheric CO_2, global SST, terrestrial carbon storage,

98 and ocean circulation have varied between the LGM and the Late Holocene, almost

99 identical $\delta^{13}C_{atm}$ values indicate that opposing effects must have offset each other (*11*). This

100 becomes clear if we look at three first-order effects on $\delta^{13}C_{atm}$: A SST rise of 1 K translates

101 into a 0.1‰ increase in $\delta^{13}C_{atm}$, due to temperature-dependent fractionation between

102 atmospheric CO_2 and marine DIC species (*12*). Assuming a global LGM-to-Holocene SST

103 rise of 3 K would result in about 0.3‰ higher $\delta^{13}C_{atm}$ for the Holocene, provided that SST

104 distribution and CO_2 gross flux exchange patterns remained constant. This effect is further

105 augmented by the uptake of isotopically light carbon by the land biosphere and

106 counterbalanced by the smaller vertical gradient in $\delta^{13}C_{DIC}$ in the Holocene ocean,

107 supported by marine data (*13*). The fact that both $\delta^{13}C_{atm}$ and CO_2 show little variation from

108 24 to 19 kyr BP points to the carbon cycle being essentially in dynamic equilibrium at that

109 time. As can also be seen in Fig. 2, the climate variations related to Heinrich stadial 2

110 (HS2) and Dansgaard-Oeschger event 2 (DO2) had little effect on the global carbon cycle

111 during this time interval. However, given the opposing trends for reconstructed atmospheric

112     $\Delta^{14}C$ ($\Delta^{14}C_{atm}$) (*14, 15*) and the expected $\Delta^{14}C_{atm}$ evolution (*16*) based on variations in ^{14}C

113   production rate (*17, 18*), the global ^{14}C budget was not balanced (Fig. 2A).

114

115   After a very small increase in $\delta^{13}C_{atm}$ at the very end of the glacial, a sharp drop in $\delta^{13}C_{atm}$

116   starting at 17.5 kyr parallels the onset of increasing atmospheric CO_2. Taken at face value,

117   this would point to an early SST rise that preceded the onset of the CO_2 increase. When we

118   apply a crude SST correction to our $\delta^{13}C_{atm}$ data based on a global estimate of SST

119   temperature changes during the transition (see SOM), this $\delta^{13}C_{atm}$ increase vanishes (Fig.

120   2B). Note, however, that this 0.06‰ excursion is within the uncertainties of our data and

121   that other effects could also lead to this small enrichment in $\delta^{13}C_{atm}$. The 0.3‰ drop in

122     $\delta^{13}C_{atm}$ after the onset of the transition at 17.5 kyr BP is accompanied by a CO_2 increase of

123   about 35 ppmv and a 190‰ drop in $\Delta^{14}C_{atm}$ (*19*), which has been attributed to a release of

124   old carbon from the deep ocean. This coeval drop in $\delta^{13}C_{atm}$ and $\Delta^{14}C_{atm}$ during the so-

125   called "mystery interval", 17.5 − 14 kyr BP (*19*), is arguably the most enigmatic carbon

126   cycle change in the course of the transition and will be discussed in more detail below.

127

128   After the broad $\delta^{13}C_{atm}$ minimum is reached at about 16 kyr BP, $\delta^{13}C_{atm}$ increases slightly

129   by 0.1‰ during the pronounced Bølling-Allerød (BA) warming. Other than circulation

130   changes in the Southern Ocean (*20*), the regrowth of the terrestrial biosphere in the northern

131   hemisphere could contribute to this increase in $\delta^{13}C_{atm}$ (*4*). However, since the SST-

132   corrected $\delta^{13}C$ evolution (Fig. 2B) does not show any increase, a robust process attribution

133   requires precisely dated SST reconstructions and transient carbon cycle modeling.

134

135   An almost linear rise by 0.06‰ per kyr follows the second $\delta^{13}C_{atm}$ minimum at 12.2 kyr

136   BP, leading to maximum values of -6.33‰ at around 6 kyr BP. This rise might be largely

137   explained by the continuing regrowth of the terrestrial biosphere (*21*), in concert with

138   smaller contributions from SST warming and changes in circulation and export production

139   (*9, 22*). From this mid-Holocene maximum, $\delta^{13}C_{atm}$ values decline slightly to reach values

140   of -6.35‰ at 0.5 kyr BP, as previously reported (*6*).

141

142   As mentioned above, the carbon cycle changes during the mystery interval have been a

143   matter of intense debate (*19, 20, 23*). Our high-resolution $\delta^{13}C_{atm}$ record together with other

144   records of carbon cycle changes and insights from models may help to constrain hypotheses

145   put forward to explain the mystery interval. The rise in CO_2 and the decline in $\delta^{13}C_{atm}$ and

146    $\Delta^{14}C_{atm}$ between 17 and 15 kyr BP fit the concept of bringing DIC-rich waters with old

147   carbon into exchange with the atmosphere. Indicative ^{14}C signals of upwelling of old, CO_2-

148   enriched deep water were found in Pacific intermediate waters (*24*), but others (*23*) ruled

149   out such old water in the northeast Pacific, and evidence for a ^{14}C-depleted glacial deep

150   ocean remains elusive (*19, 23, 25*). These $\Delta^{14}C$ studies were usually confronted with

151   variable reservoir age between benthic and planktonic foraminifera. A study using deep sea

152   corals now circumvents this problem by applying absolute U-Th dating and shows that the

153   deep glacial Southern Ocean indeed ventilated its ^{14}C-depleted reservoir during the mystery

154   interval (*26*).

155

156   The constant $\delta^{13}C_{atm}$ values during the late glacial indicate that the build-up of such an old,

157   DIC-rich reservoir must have occurred before 24 kyr BP. A large number of records mark

158   the start of the deglaciation around 17 kyr BP (Fig. 2). Within the uncertainty in marine and

159   ice core age scales, the CO_2 increase, the pronounced $\Delta^{14}C_{atm}$ drop (*15*), the resumption of

160   vigorous Southern Ocean upwelling as recorded in intense deposition of biogenic opal (*20*),

161   and the launch of ice-rafted debris layers at the beginning of the Heinrich 1 stadial (*27*) all

162   occurred simultaneously. Interestingly, our $\delta^{13}C_{atm}$ record shows its largest deviation of

163   0.3‰, i.e. the entire $\delta^{13}C_{atm}$ decrease from the LGM to the Preboreal (PB), within the first 2

164   kyr after the start of the deglaciation. Within the same interval, CO_2 rose by 30 ppmv from

165   190 ppmv to 220 ppmv, i.e. only 35% of the LGM-PB rise. Together with the trend reversal

166   in $\delta^{13}C_{atm}$ towards the end of the mystery interval, this indicates that only a fraction of the

167   glacial/interglacial CO_2 increase can be explained by an intensification of deep ocean

168   ventilation bringing isotopically depleted and carbon-rich water to the surface of the

169   Southern Ocean. Our new, high-resolution $\delta^{13}C_{atm}$ data constrain the period of this release

170   of isotopically depleted carbon from the deep ocean to the atmosphere to between 17.4 kyr

171   BP and 15 kyr BP. This interpretation of the proxy records is quantitatively in line with

172   dynamical ocean model results that link deep ocean ventilation, atmospheric CO_2, $\delta^{13}C_{atm}$,

173    $\delta^{13}C_{DIC}$, opal burial, and radiocarbon (*28*).

174

175   Alternative hypotheses (*29, 30*) invoking the release of old carbon from permafrost or

176   carbon locked under continental ice sheets are unlikely to explain the carbon cycle changes

177   in the mystery interval because the amount of terrestrial carbon needed to account for the

178 ^{14}C drop is very large, at 5000 Gt (*25*), and would conflict with the moderate 30 ppmv rise

179 in atmospheric CO_2. Moreover, it would lead to an overall decline in $\delta^{13}C_{DIC}$, which is not

180 observed in benthic foraminifera in the deep ocean (*13, 22*). Also, a carbonate dissolution

181 event at the sea floor that would have to accompany such a large terrestrial carbon release

182 into the atmosphere/ocean system is not imprinted in the deglacial marine $CaCO_3$ record

183 (*31*)

184

185 Consequently, despite the fact that the search for an extremely ^{14}C-depleted deep water

186 mass in marine records has thus far not been successful (*23*) and might not even essential to

187 explain the $\Delta^{14}C_{atm}$ anomaly (*26*), the release of carbon from the deep ocean remains the

188 most plausible scenario to explain the early deglacial drop in our new $\delta^{13}C_{atm}$ record.

189 Furthermore, model results suggest that a $\delta^{13}C_{atm}$ decrease of 0.3‰ and a CO_2 increase of

190 about 30 ppmv can be accommodated by relatively small (about 20‰) and spatially

191 complex changes in deep ocean $\Delta^{14}C$ (*28*). These changes may remain undetected in the

192 search for the old abyssal water using benthic foraminifera (*19, 25*). However, they are also

193 too small to explain the reconstructed $\Delta^{14}C_{atm}$ decline in the mystery interval. Based on

194 these considerations, the currently available marine and ice core information cannot be

195 reconciled with the atmospheric radiocarbon record in a straightforward manner. One

196 possibility to resolve this issue is to also reconsider a larger change in ^{14}C production

197 between the Holocene and the glacial, and to work towards independent verification of the

198 $\Delta^{14}C_{atm}$ history.

199

199   **References and Notes:**

200   1.   D. Lüthi *et al.*, Nature **453**, 379 (2008).
201   2.   H. Fischer *et al.*, Quat. Sci. Rev. **29**, 193 (2010).
202   3.   E. Monnin *et al.*, Science **291**, 112 (2001).
203   4.   P. Köhler, H. Fischer, G. Munhoven, R. E. Zeebe, Global Biogeochem. Cycles **19**,
204   GB4020 (2005).
205   5.   D. M. Sigman, M. P. Hain, G. H. Haug, Nature **466**, 47 (2010).
206   6.   J. Elsig *et al.*, Nature **461**, 507 (2009).
207   7.   H. J. Smith, H. Fischer, M. Wahlen, D. Mastroianni, B. Deck, Nature **400**, 248
208   (1999).
209   8.   M. Leuenberger, U. Siegenthaler, C. C. Langway, Nature **357**, 488 (1992).
210   9.   A. Lourantou *et al.*, Global Biogeochem. Cycles **24**, GB2015 (2010).
211   10.   J. Schmitt, R. Schneider, H. Fischer, Atmos. Meas. Tech. **4**, 1445 (2011).
212   11.   P. Köhler, H. Fischer, J. Schmitt, Paleoceanography **25**, PA1213 (2010).
213   12.   J. Zhang, P. D. Quay, D. O. Wilbur, Geochim Cosmochim Ac **59**, 107 (1995).
214   13.   K. I. C. Oliver *et al.*, Clim. Past **6**, 645 (2010).
215   14.   P. J. Reimer *et al.*, Radiocarbon **51**, 1111 (2009).
216   15.   J. Southon, A. L. Noronha, H. Cheng, R. L. Edwards, Y. Wang, Quat. Sci. Rev. **33**,
217   32 (2012).
218   16.   P. Köhler, R. Muscheler, H. Fischer, Geochem. Geophys. Geosyst. **7**, Q11N06
219   (2006).
220   17.   C. Laj, C. Kissel, J. Beer, in *Timescales of the Paleomagnetic Field*. (American
221   Geophysical Union, 2004), vol. 145, pp. 255-265.
222   18.   R. Muscheler, R. Beer, P. W. Kubik, H. A. Synal, Quat. Sci. Rev. **24**, 1849 (2005).
223   19.   W. Broecker, S. Barker, Earth Planet. Sci. Lett. **256**, 90 (2007).
224   20.   R. F. Anderson *et al.*, Science **323**, 1443 (2009).
225   21.   P. Ciais *et al.*, Nat. Geosci **5**, 74 (2012).
226   22.   J. M. Yu *et al.*, Science **330**, 1084 (2010).
227   23.   D. C. Lund, A. C. Mix, J. Southon, Nat. Geosci. **4**, 771 (2011).
228   24.   L. Stott, J. Southon, A. Timmermann, A. Koutavas, Paleoceanography **24**, PA2223
229   (2009).
230   25.   W. Broecker, E. Clark, Geophys. Res. Lett. **37**, L13606 (2010).
231   26.   A. Burke, L. F. Robinson, Science **335**, 557 (2012).
232   27.   E. Bard, F. Rostek, J. L. Turon, S. Gendreau, Science **289**, 1321 (2000).
233   28.   T. Tschumi, F. Joos, M. Gehlen, C. Heinze, Clim. Past **7**, 771 (2011).
234   29.   R. Zech, Y. Huang, M. Zech, R. Tarozo, W. Zech, Clim. Past **7**, 501 (2011).
235   30.   N. Zeng, Clim. Past **3**, 135 (2007).
236   31.   D. A. Hodell, C. D. Charles, F. J. Sierro, Earth Planet. Sci. Lett. **192**, 109 (2001).
237   32.   B. Lemieux-Dudon *et al.*, Quat. Sci. Rev. **29**, 8 (2010).
238   33.   North Greenland Ice Core Project members, Nature **431**, 147 (2004).
239   34.   EPICA Community Members, Nature **444**, 195 (2006).
240   35.   B. Stenni *et al.*, Science **293**, 2074 (2001).
241   36.   J. Elsig, Dissertation, University of Bern (2009).
242   37.   D. Lüthi *et al.*, Earth Planet. Sci. Lett. **297**, 226 (2010).

243 38. G. Dreyfus, Phd Thesis, Princeton University (2008).
244 39. G. B. Dreyfus *et al.*, Quat. Sci. Rev. **29**, 28 (2009).
245 40. R. J. Francey *et al.*, Tellus **51B**, 170 (1999).
246 41. R. Spahni *et al.*, Geophys. Res. Lett. **30**, 25 (2003).
247 42. D. Buiron *et al.*, Clim. Past **7**, 1 (2011).
248 43. I. G. Enting, J. Geophys. Res.-Atmos. **92**, 10977 (1987).
249 44. J. Schwander, B. Stauffer, A. Sigg, Annals of Glaciology **10**, 141 (1988).
250 45. A. Indermühle *et al.*, Nature **398**, 121 (1999).
251 46. R. E. Zeebe, D. A. Wolf-Gladrow, *CO₂ in seawater: equilibrium, kinetics, isotopes*,
252   Elsevier Oceanography series (2005), pp. 65.
253 47. P. M. Grootes, M. Stuiver, J. Geophys. Res.-Oceans **102**, 26455 (1997).
254 48. J. Jouzel *et al.*, Science **317**, 793 (2007).
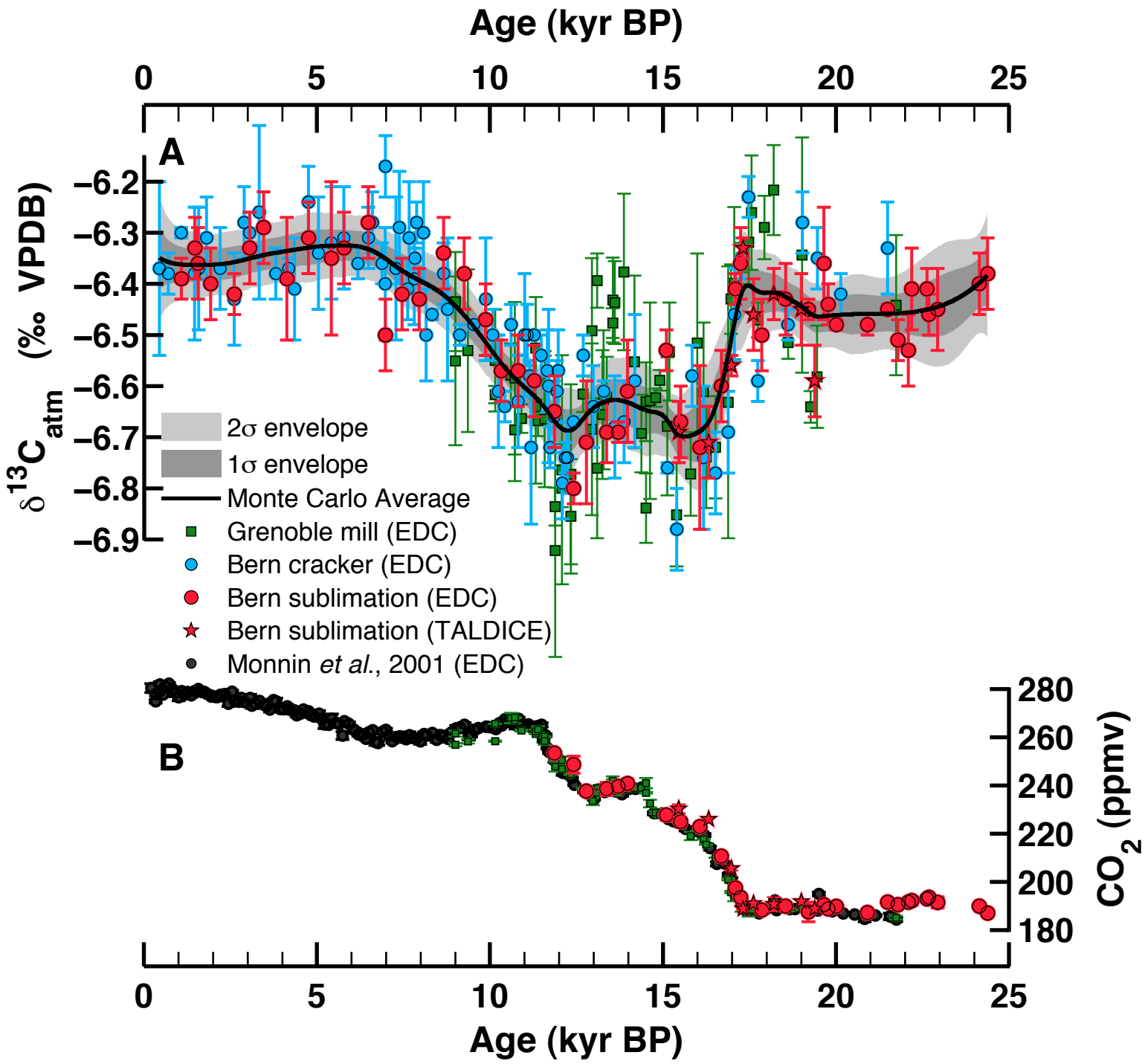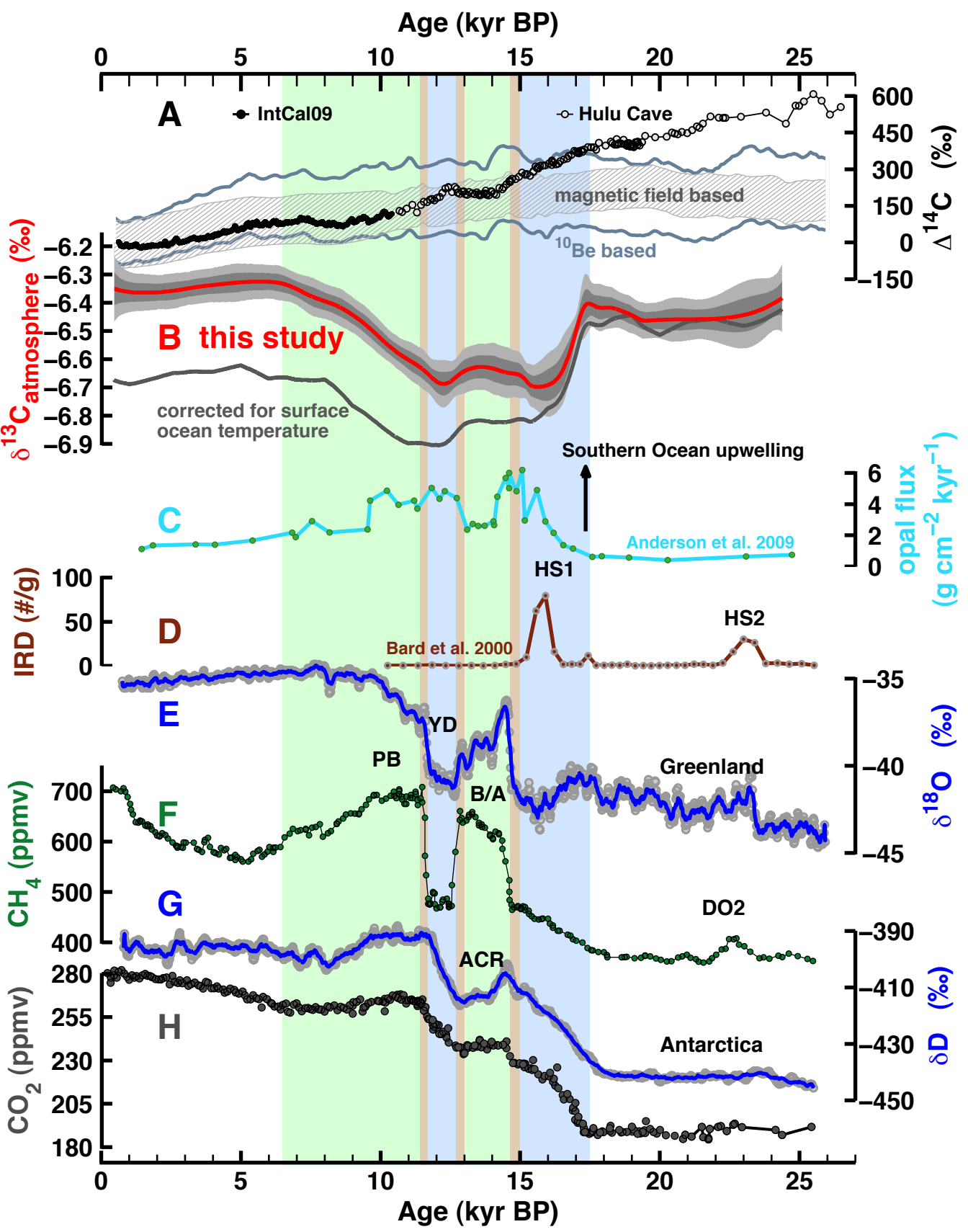255 49. K. Visser, R. Thunell, L. Stott, Nature **421**, 152 (2003).
256
257

273　**Fig. 1.** Ice core reconstructions of atmospheric $\delta^{13}C$ and CO_2 concentration covering the

274　last 24 kyr. (**A**) $\delta^{13}C_{atm}$ of atmospheric CO_2 measured with three different methods on two

275　different ice core drill sites. Blue circles: Bern cracker data, green squares: Grenoble mill

276　data (*9*) after offset correction, red circles: Bern sublimation data. Red stars indicate values

277　from the sublimation method but measured on Talos Dome Ice Core (TALDICE). Error

278　bars represent the standard deviation of replicate measurements. The black line is the result

279　of 4000 Monte Carlo simulations representing an error-weighted average of the different

280　$\delta^{13}C_{atm}$ data sets. The light and dark shaded areas represent the 2σ and 1σ error envelope

281　around the Monte Carlo Average (see SI). (**B**) CO_2 concentration. Black circles represent

282　earlier measurements on EDC (*3*), other symbols are the same as in panel **A**. Note: All ice

283　core records are plotted on a synchronized age scale (*32*).

284

284   **Fig. 2.** Ice core reconstructions and marine records illustrating the evolution of major

285   components of the Earth climate system over the last 24 kyr. (**A**) Reconstructed $\Delta^{14}C_{atm}$

286   from IntCal09 (*14*) and the ^{230}Th-dated Hulu Cave $\Delta^{14}C_{atm}$ record (*15*) compared with

287   modeled (*16*) $\Delta^{14}C_{atm}$ assuming a constant carbon cycle under pre-industrial conditions but

288   considering temporal changes in ^{14}C production (either based on ^{10}Be (*18*), upper and lower

289   estimates enveloped in gray lines, or on paleomagnetic field intensity (*17*), hatched area).

290   (**B**) Monte Carlo simulations (this study) of the evolution of $\delta^{13}C_{atm}$ before (red line

291   represents the MCA, 2σ and 1σ envelopes are in gray) and after SST correction (gray line;

292   see SI) (**C**) Opal flux in the Southern Ocean as a proxy for local upwelling (*20*). (**D**) Record

293   of ice rafted debris (IRD) in the North Atlantic associated with Heinrich stadials (HS1 and

294   HS2) (*27*). (**E**) Greenland temperature proxy $\delta^{18}O$ (*33*). (**F**) Reconstructed atmospheric CH_4

295   concentration (*34*) (**G**) Antarctic temperature proxy δD from the EDC ice core (*35*). (**H**)

296   Compilation of reconstructed CO_2 shown in Fig. 1B. Green bars indicate intervals with a

297   strong net terrestrial carbon build-up, blue bars indicate intervals where sequestered deep

298   ocean CO_2 was released back to the atmosphere. Note: Ice core records are plotted on a

299   synchronized age scale (*32*), other records are plotted on their individual age scales.

300

A

$\delta^{13}C_{atm}$ (‰ VPDB)

Age (kyr BP)

2σ envelope
1σ envelope
Monte Carlo Average
Grenoble mill (EDC)
Bern cracker (EDC)
Bern sublimation (EDC)
Bern sublimation (TALDICE)
Monnin *et al.*, 2001 (EDC)

B

CO_2 (ppmv)

Supporting Online Material for

Carbon isotope constraints on the deglacial CO_2 rise from ice cores

Jochen Schmitt, Robert Schneider, Joachim Elsig, Anna Lourantou, Daiana Leuenberger,
Jérôme Chappellaz, Peter Köhler, Fortunat Joos, Thomas Stocker, Markus Leuenberger,
Hubertus Fischer

correspondence to: schmitt@climate.unibe.ch

This PDF file includes:

Materials and Methods

Analysis of $\delta^{13}C$ on ice core samples

The measurement of $\delta^{13}C$ on ice core samples follows well-established protocols which have been applied in other studies (*6, 9, 10, 35*). In short, all three methods rely on four main steps. First, enclosed atmospheric air from the ice sample is released using a dedicated extraction device (sublimation, needle cracker and a ball mill for the respective data sets: Bern sublimation, Bern cracker and Grenoble mill). In a second step, the CO_2 from the released ice core air is separated from the bulk air (N_2, O_2 and Ar) using cryogenic trapping. Third, a gas chromatographic column purifies the CO_2 sample from other trace gases such as N_2O. Finally, the stable carbon isotopic ratio of the CO_2 sample is measured against a bracketing standard using an isotope ratio mass spectrometer. The typical measurement reproducibilities of the three methods are 0.05‰ - 0.07‰ for the Bern sublimation (*6, 10*), 0.07‰ for the Bern cracker (*6*), and 0.10‰ for the Grenoble mill data set (*9*). Note that the method used for the Bern sublimation data set employs a novel sublimation technique (*10*). Besides a somewhat better prevision, this technique offers the unique advantage of a quantitative gas extraction from the ice sample. The two other methods use conventional mechanic extraction devices (mill or cracker techniques), which extract only around 80% of the enclosed air in samples consisting of bubbly ice (usually the upper part, i.e. <600 m depth, of a deep ice core). This may become more problematic for ice from the bubble clathrate transition zone, where fractionation between different gases has been observed for incomplete gas extraction (*36*). Here we use only deglacial ice from Dome C located in the pure bubble zone and no gas extraction effects are to be expected for any extraction method used.

Gravitational correction of the $\delta^{13}C$ data

Since gases and their isotopes become fractionated in the diffusive firn column due to gravitational fractionation, the measured $\delta^{13}C$ values must be corrected for gravitational enrichment to derive the atmospheric signal ($\delta^{13}C_{atm}$). To do this, measured $\delta^{15}N$ on N_2 serves as a proxy for the gravitational enrichment of the stable carbon isotopes of CO_2. This approach can be used because the isotopic composition of N_2 was constant over the covered time interval, and the gravitational fractionation is only dependent on the mass difference, Δm, of the molecules, i.e. $\Delta m = 1$ for both $\delta^{15}N$ and $\delta^{13}C$. The three data sets (Bern sublimation, Bern cracker, and Grenoble mill) were corrected using the same measured $\delta^{15}N$ data set provided by Dreyfus (*37*) and by following previously published procedures (*6, 9, 35*). The typical gravitational enrichment for the EDC core ranges between 0.42‰ for glacial samples and 0.52‰ for Holocene samples. The reproducibility of the $\delta^{15}N$ measurements is about 0.01‰ (*37*).

As the $\delta^{15}N$ measurements and $\delta^{13}C$ measurements are not carried out on exactly the same ice core sample nor at the same temporal resolution, an interpolation step must

first be performed. To prevent all measurement noise of $\delta^{15}N$ data from being transferred to the reconstructed $\delta^{13}C_{atm}$ record, a spline interpolation is used, which is superior to a point-to-point interpolation for reasons discussed by Elsig (*35*). A second approach makes use of an empirical relation between $\delta^{15}N$ and the water isotopic composition δD, which serves a proxy for relevant firn processes, i.e. accumulation rate, thickness of the diffusive column height and firn temperature (*38*). This $\delta^{15}N$-δD relation must be applied for time periods where $\delta^{15}N$ measurements are not available, which is the case for the time interval between 24 kyr and 22 kyr. As the glacial-interglacial shift of $\delta^{15}N$ for the EDC ice core is only 0.1‰ and the $\delta^{15}N$-δD relation explains 88% of the variability (*38*), the differences between the two approaches to correct for gravitational fractionation are negligible compared to the reproducibility of the $\delta^{13}C$ measurement. Since the measurement reproducibility of $\delta^{15}N$ is with 0.01‰ much lower than for $\delta^{13}C$, the introduced error is between 0.01 and 0.02‰ and mainly due the interpolation procedure described above.

The ice core measurements and the calculated Monte Carlo Average are available at: http://doi:10.1594/PANGAEA.772713

Extracting the atmospheric signal

The following procedure describes the stepwise statistical data analysis to combine the three individual data sets ("residual analysis") and to derive a robust atmospheric signal ("Monte Carlo spline process"). These steps make use of a bootstrap procedure to account for the specific measurement precision among the data sets and to allow for identification of outliers, i.e. data points which are incompatible with the common atmospheric signal in the data set.

Residual analysis

In the main text, we combine three independently measured $\delta^{13}C_{atm}$ data sets of different precision, accuracy and resolution for the last 24 kyr. A unified $\delta^{13}C_{atm}$ time series of the three individual time series has to account for offsets among the records as well as for the individual measurement precision.

In the following, we quantify the overall differences in accuracy between the records. As our sublimation data (*6*) agree well with measurements from the Law Dome ice core (*39*), which have an overlap with firn air reconstructions and archived air from the Cape Grim air archive, we set the sublimation data as the reference (for details see discussion in Schmitt et al., 2011 (*10*)). To account for this agreement with the Law Dome record (*39*), the overlapping period of the Law Dome record is added to the combined data set for the Monte Carlo spline routine as additional data point (see Fig. S4). In the first step, the potential offsets between the Bern sublimation data to the Bern cracker data and the data from the Bern sublimation to the Grenoble mill are analyzed and quantified. As the procedure is the same for the Bern cracker and Grenoble mill data sets, we generally outline an offset calculation for the Bern sublimation to a 'non-

sublimation' data set. In principle, residual $\delta^{13}C$ values between two datasets are determined where they overlap. The resulting mean systematic difference is called offset and represents the difference in the accuracy of the methods. However, the individual ice samples of the three data sets are not measured at exactly the same depth, hence gas age, which complicates direct calculation of the $\delta^{13}C$ residuals. For each data point of a non-sublimation record, we choose the nearest available Bern sublimation data point in time. The overall mean time difference between compared points is $\Delta t = 29 \pm 171$ years for the Bern cracker and $\Delta t = 34 \pm 175$ years for the Grenoble mill data set (Fig. S1B and S2B). This Δt is sufficiently small compared to the width of the gas age distribution in EDC and Talos Dome ice (*40, 41*). This is also illustrated in Fig. S1B and S2B, which show that the absolute values of the residuals do not increase with larger Δt. Hence, we can safely assume that the differences in the compared data points arise essentially from differences in the accuracy and precision in all three methods. The calculated individual $\Delta\delta^{13}C$ residuals are sorted into bins and plotted in a histogram.

Performing a Gaussian fit yields the mean offset and the standard deviation between sublimation and non-sublimation data set. To account for the relatively small sample number for the residual distribution we performed a Monte Carlo procedure to determine the mean and standard deviation of the distribution. In a first Monte Carlo iteration, the procedure is repeated 100 times, randomly varying the input data within their 1σ standard deviation. From each of the obtained 100 Monte Carlo runs, a Gaussian fit is calculated providing a mean offset and 1σ standard deviation after averaging over the 100 runs. Figure S3 shows the histogram of the residuals for the Bern cracker (A) and the Grenoble mill (B) data set. On top of the histogram, a Gaussian distribution is drawn using the average mean and standard deviation from the fitted distributions of the 100 Monte Carlo runs.

If the residuals are only due to the stochastic measurement errors in the two methods compared, then their distribution has to be Gaussian with the width of the distribution given by the propagated error of both methods. This is perfectly fulfilled for the residuals between the Bern sublimation and Bern cracker data (Fig. S3A). For the Bern cracker record, the calculated offset of -0.01‰ ± 0.11‰ to the sublimation record is very small and in line with a similar analysis done on the Holocene data set (*6*). The distribution of the residuals is Gaussian, and its width can be entirely explained by error propagation of the individual measurement error of both methods. For the Grenoble mill data the distribution is reasonably Gaussian but the width is slightly larger than expected from the propagated measurement errors. An offset of 0.16‰ ± 0.17‰ between the Grenoble mill data and the Bern sublimation data is observed and correcting for this offset improves the combined record. To apply a constant offset correction, the offset has to be constant with time. Therefore, we performed a second analysis for the case of the $\Delta\delta^{13}C$ residuals varying with time. Fig. S1A and Fig. S2A show these residuals as a function of the age of the respective data point. The Bern cracker data shows no temporal dependence of the offset, the Grenoble mill data shows a slight tendency to higher offsets for younger ages (higher CO_2 concentrations), however, this trend is statistically not significant. Due to the small sample number available for the residual analysis we refrained from correcting this insignificant trend. Instead we only shifted the Grenoble data set by its mean offset relative to the Bern sublimation data. The three involved labs in Bern and Grenoble also

conducted a round-robin exercise with three cylinders with working standards to identify possible scale differences among the labs. For the cylinders, we also measured offsets which range in the observed differences among Bern and Grenoble ice core data. We could not completely identify the reasons for these small differences. Note that in view of the complex analytical systems and the differences in the referencing strategy of the three methods, the observed systematic offsets are to be expected, rather small and reproducible.

We acknowledge that the posteriori offset procedure introduces a systematic additional error to the Grenoble data set. However, we did not add this "offset error" to the measurement error since the Monte Carlo procedure would then put even less weight onto this data set and the calculated spline would be more biased towards the Bern data sets. Note that the outcome of the Monte Carlo spline procedure described below, is not significantly affected by the inclusion of the Grenoble mill data and that all of the conclusions drawn in our paper also hold, if that data set were to be excluded. However, inclusion of all three data sets is essential to obtain the highest temporal resolution possible for the $\delta^{13}C_{atm}$ record.

Calculating Monte Carlo splines of the combined record

In a second step after the offset correction, cubic splines (*42*) of the combined $\delta^{13}C_{atm}$ time series were calculated. To exclude the high frequency measurement noise, splines with a cut-off period of 375 years were selected (see Fig. S4 showing 400 sample splines). This value was chosen as for the ice cores used in this study, variability on shorter time periods is strongly dampened in gas reconstructions due to the low-pass filtering of the primary atmospheric signal by the continuous bubble enclosure process in the firn column (*43*). The spline calculation is repeated 4000 times, with the input data randomly picked from their 1σ error range. For replicate samples, the 1σ standard deviation of these specific data points is used. In the case that the 1σ standard deviation for replicate samples is better than the mean reproducibility of the method, the mean standard deviation of the data set is used. The same applies for points where only one ice sample was measured. Assigning the mean standard deviation of the data set to those data points prevents unjustified pinning of the spline evolution at these positions. As can be seen in Fig. S4 and S5, regions where data points have small error bars tend to pin the spline evolution (e.g., compare spline evolution in Fig. S4 at position (D) and the respective distribution in Fig. S5D). The arithmetic average, here called the Monte Carlo Average (MCA), is calculated from the 4000 splines. Due the variability of the individual splines, the calculated MCA is smoother than the individual splines (Fig. S4). This additional smoothing of the MCA is a function of the measurement precision of a data point and its temporal distance to its neighbors (i.e. temporal resolution). Since neither the individual records nor the combined data set are equidistant and the measurement error varies among the data sets and with time, the additional smoothing of the MCA varies with time (Fig. S4). In other words, the MCA cannot be characterized by a defined cut-off period. Instead, our procedure removes high frequency components of the splines at positions where these were not robust enough as measurement error and temporal resolution did not allow to constrain the individual splines sufficiently. On the other

hand, for time intervals with small error bars and dense data coverage, the individual splines are pinned. Here, the resulting distribution is narrow, and the high frequency components were retained (Fig. S5D). This procedure is superior to approaches calculating only one spline with a fixed cut-off period, hence constant smoothing characteristic, as the MCA can account for inhomogeneous measurement error and variable temporal resolution, a common feature of our data sets. Finally, the dark gray (light gray) shaded envelopes in Fig. 1 and 2 are obtained, marking the 1σ (2σ) confidence interval of the Monte Carlo average. As the distributions of the splines at a given point in time are not truly Gaussian (see example histograms in Fig. S5), the 1σ and 2σ confidence intervals serve as approximations for the true spline variability at each point in time. Table S3 provided digitally in the supplement lists the MCA and the 1σ envelope on the synchronized age scale (*31*).

To investigate the robustness of the chosen approach to combine the three data sets, we also calculated MCAs for subsets of the combined data. Four cases are selected and shown in Fig. S6. In case A we tested if the outlier detection does actually improve or alter the MCA (see discussion below). As illustrated in Fig. S6A this is not the case. Case B is calculated without the TALDICE samples (which have a different gas age distribution than Dome C samples) and shows that removing this subset does not change the MCA. Removing the Grenoble subset in case D leads to only minor changes in the MCA between 12-15 kyr BP. When the MCA is calculated from the sublimation data only, the spline routine produces more wiggles as the temporal resolution of the sublimation data alone is not sufficient for this cut-off period. However, also in this extreme case the general shape of the MCA is still preserved and the MCAs agree within their 2σ envelopes. This analysis shows that combining the two Bern data sets and the Grenoble data set is a beneficial approach as it increases the temporal resolution and provides a more robust result but does not create spurious trends.

Outlier detection with bootstrapping

Atmospheric stable carbon isotope measurements on the EDC ice core over the Holocene report a significant measurement outlier at 170 m depth, that can neither be explained by a climatic excursion nor by poor measurement precision, but is likely caused by problems during the ice core drilling (*6*). To test for further outliers in the combined data set, the above described Monte Carlo procedure is repeated, but each time one data point is excluded. If the calculated 2σ confidence interval of the MCA does not overlap with the 2σ error of the excluded data point, this data point is assigned as an outlier and excluded from the final spline calculation. This test is done for all data points, resulting in only four measurements excluded from the data set. Note that for this bootstrap procedure, all individual measurements were used instead of the replicate mean. In a last step, the bootstrap procedure was repeated using also the replicate means instead of the individual replicates. No data point was identified as an outlier during this final step. Since only four individual measurement points were identified as outlier, the calculated MCA is not dependent on whether the outliers are included or excluded during the Monte Carlo procedure as the respective MCA and 2σ confidence intervals nicely overlap (Fig. S6A). In summary, if a data point cannot be identified a priory as an artifact

due to either measurement problems or during drilling (e.g. the 170 m depth outliers in the Holocene section) the bootstrap procedure does not improve the MCA. In other words, the observed scatter in the combined data set can be explained already by the combined measurement error and errors due to offset corrections.

Correction for SST changes

With changing sea surface temperature (SST), not only the partial pressure of dissolved CO_2 in water (pCO_2) but also the isotopic fractionation during the gas exchange is altered. The $\delta^{13}C$ of atmospheric CO_2 becomes isotopically heavier by roughly 0.1‰ per 1 K increase as the fractionation factor decreases (*12, 44, 45*). In the following, we attempted to roughly quantify this effect of changing SST on $\delta^{13}C_{atm}$ over the transition.

The temperature at 19 kyr BP is set as a reference point, as changes in global mean sea surface temperature at earlier glacial times are small compared to the variations during the glacial termination. The isotopic ratio of atmospheric CO_2 Δt years after 19 kyr BP is calculated according to:

$$\delta^{13}C\ (19\ kyr\ BP + \Delta t) = \delta^{13}C\ (19\ kyr\ BP) + \Delta(\delta^{13}C), \qquad (1)$$

where

$$\Delta(\delta^{13}C) = \alpha\ \Delta T,\ with\ \alpha = 0.1‰/K. \qquad (2)$$

The evolution of the past global mean SST can be approximated from direct marine proxies, such as alkenones or Ca/Mg ratios. For regions and time periods without marine proxy records, scaled temperature evolutions of Greenland and Antarctica serve as crude representations of the surrounding oceans. In the course of this work, we use the estimations compiled by Köhler et al. (*4*) that have been used in other modeling studies (*11*). In this compilation, the surface ocean is divided into five regions (corresponding to the surface boxes used in Köhler et al. (*4*)): the North Atlantic, the Equatorial Atlantic, the Southern Ocean, the Equatorial Indo-Pacific and the North Pacific. For each box, temperature proxies are used to account for the change in SST. The stable water isotopic signal $\delta^{18}O$ from the GISP2 (*46*) and δD from the EDC (*47*) ice cores were rescaled to a glacial/interglacial amplitude of 4 K and used to quantify the SST evolutions of the Northern boxes and the Southern Ocean, respectively. Temperature changes in lower latitude boxes were adapted from foraminifera records (*48*). The SST approximations for the five surface boxes are shown in Fig. S7B (equatorial boxes) and Fig. S7C (high latitude boxes), together with the area-weighted temperature average (gray curve in Fig. S7B). Note that gas exchange and thus the isotopic fractionation are largely inhibited for sea-ice covered areas. Therefore, only areas dominated by open water were used for the calculation of the area-weighted SST average. These areas are calculated internally within the BICYCLE model (*4*). Accounting for the change in sea-ice area leads to a difference of only 0.8 K in the area-weighted SST estimate over the period between 19 kyr and 10 kyr. The total shift from 19 kyr BP to the Holocene in this reconstruction is 2.8 K.

This global SST record is used to calculate the SST-corrected evolution of $\delta^{13}C_{atm}$ according to equations (1) and (2) (gray line in Fig. S7A) by subtracting the SST-induced $\delta^{13}C$ change from the Monte Carlo Average (red line in Fig. S7A). We note that our temperature approximation introduces further error to the one and two sigma confidence interval of the SST corrected record. However, a detailed error propagation analysis is beyond the scope of the overall approximation since the purpose of this correction was to provide only a rough estimate of the global SST change on our $\delta^{13}C_{atm}$ record, i.e. to show that global SST changes likely shift the $\delta^{13}C_{atm}$ by approximately 0.3‰ from the LGM to the Holocene. Note also that the proxies used for our crude SST reconstruction are on their individual age scales; therefore, interpretations on the submillennial timescale are not possible. For illustration purposes, we also assumed a simple linear SST increase of 2.8 K between 19 kyr and 10 kyr and a constant SST during the Holocene (Fig. S7B). The resulting $\delta^{13}C$ anomaly was subtracted from the $\delta^{13}C_{atm}$ evolution of the MCA, and this simple linear SST rise correction (Fig. S7A blue and orange line) is compared with the proxy-based SST correction. As the proxy based mean SST evolution during the deglaciation is already rather linear with only small deviations during the YD-BA oscillation, the two SST reconstructions are similar as well. In summary, our SST correction serves as an illustration of the effect of an overall glacial/interglacial warming, while small scale features in the corrected $\delta^{13}C_{atm}$ record on sub-millennial time scale should not be interpreted.
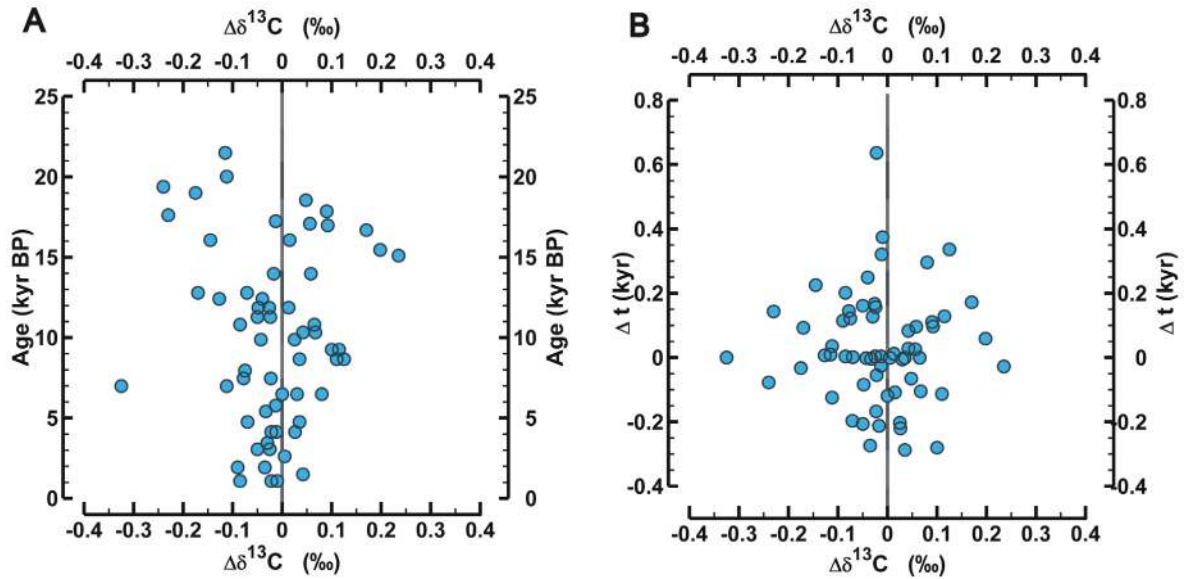
Fig. S1.

Residual plots for the Bern cracker data set. **(A)** Residuals plotted against the absolute age of the Bern cracker measurements. The data points are randomly scattered around the zero line showing no trend with time. However, the scatter shows a tendency to become larger for glacial ice with lower CO_2 concentration. **(B)** Residuals plotted against Δt, i.e. the temporal difference between a Bern cracker measurement to its nearest neighbor in the Bern sublimation data. Most Δt values lie between +0.2 kyr and -0.2 kyr, with no trend of larger $\Delta\delta^{13}C$ residuals for larger Δt differences.
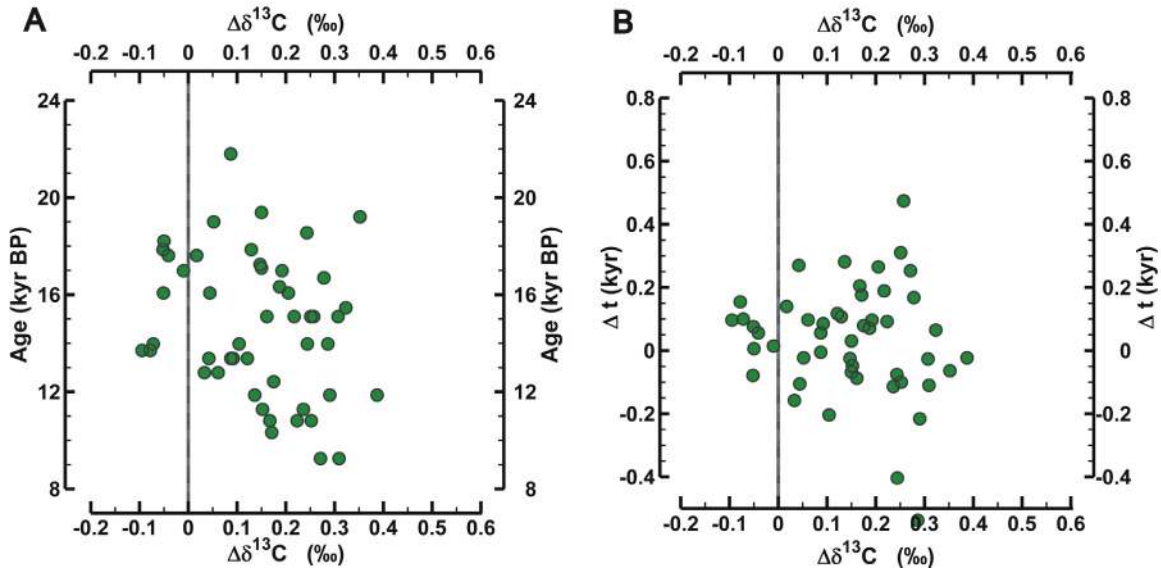
Fig. S2

Residual plots for the Grenoble mill data set. **(A)** Residuals plotted against the absolute age of the Grenoble mill measurements. The data points are randomly scattered but show an offset to the zero line. **(B)** Residuals plotted against Δt, i.e. the temporal difference between a Grenoble mill measurement to its nearest neighbor in the Bern sublimation data. Most Δt values lie between +0.2 kyr and -0.2 kyr, with no trend of larger $\Delta\delta^{13}C$ residuals for larger Δt differences.
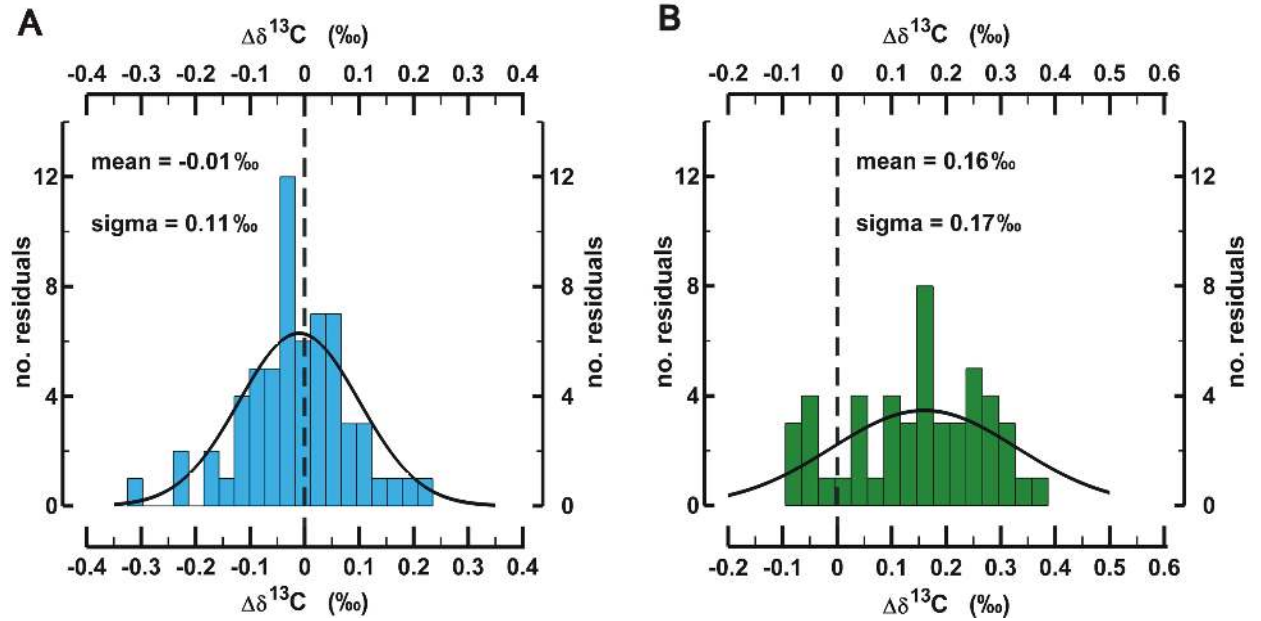
Fig. S3

Histograms showing the offsets among the data sets: The histograms show the residuals of the measured mean value at a given sample depth for the Bern cracker **(A)** and the Grenoble mill **(B)** data sets to its nearest neighbor in the Bern sublimation data. The output of a Monte Carlo procedure (see text) was used to determine the mean and standard deviation of the Gaussian curve (black line).
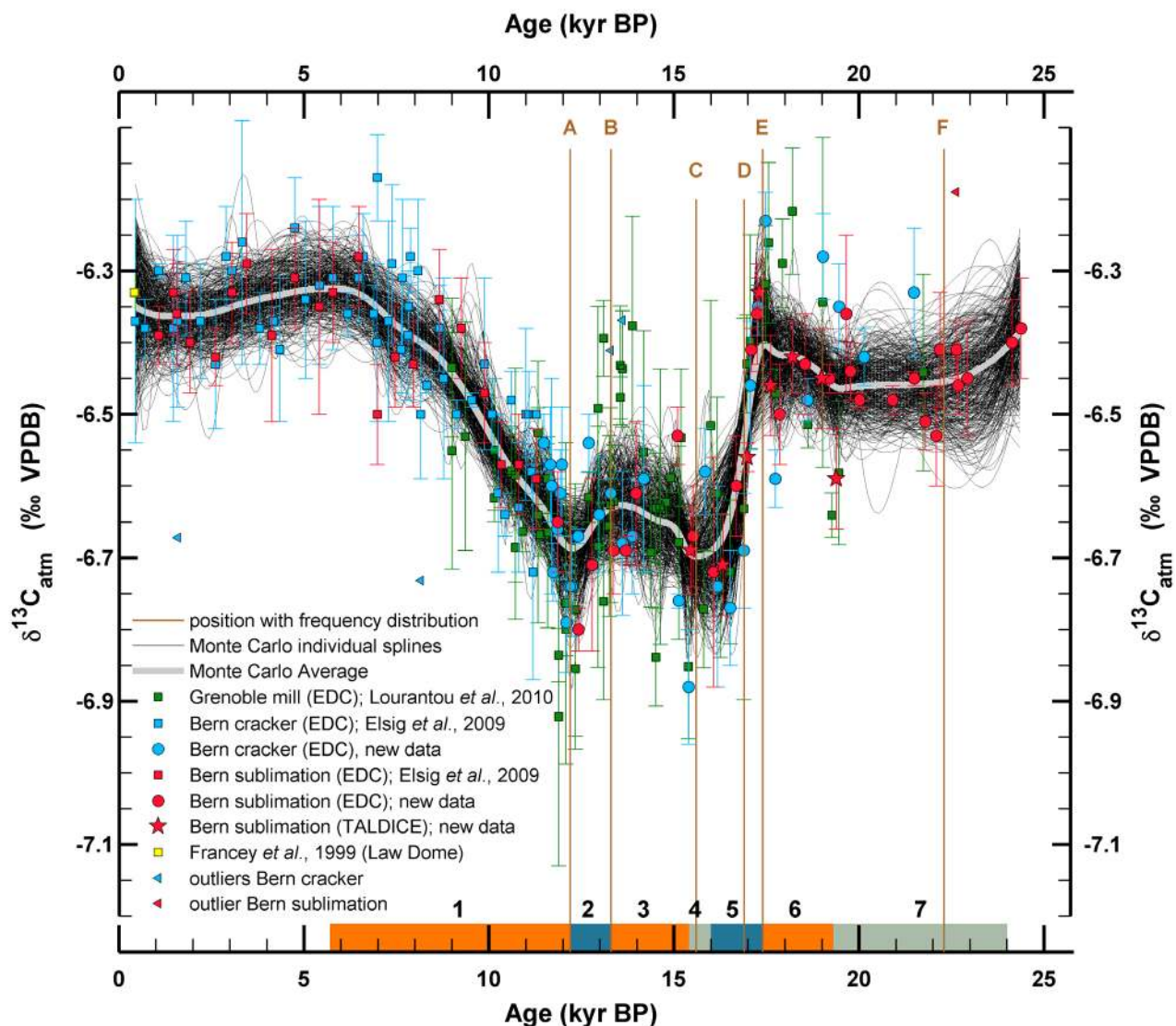
Fig. S4

Individual Monte Carlo splines: Compilation showing the color-coded $\delta^{13}C_{atm}$ measurements. Squares indicate published data, circles new measurements, and triangles denote individual data points which were detected as outliers in the bootstrap routine. The Monte Carlo Average is plotted in gray and in black a sample of 400 Monte Carlo splines with a cut-off period of 375 years. Latin letters A to F connected to vertical lines denote time intervals where the frequency distribution of the 4000 splines is shown in Fig. S5. Numerals from 1-7 at the bottom axis mark the time intervals shown in Tab. S2. All $\delta^{13}C_{atm}$ records from this study are on a synchronized age scale (*31*); only the reference data point at 0.42 kyr from the Law Dome record (*39*) is on its original age scale.
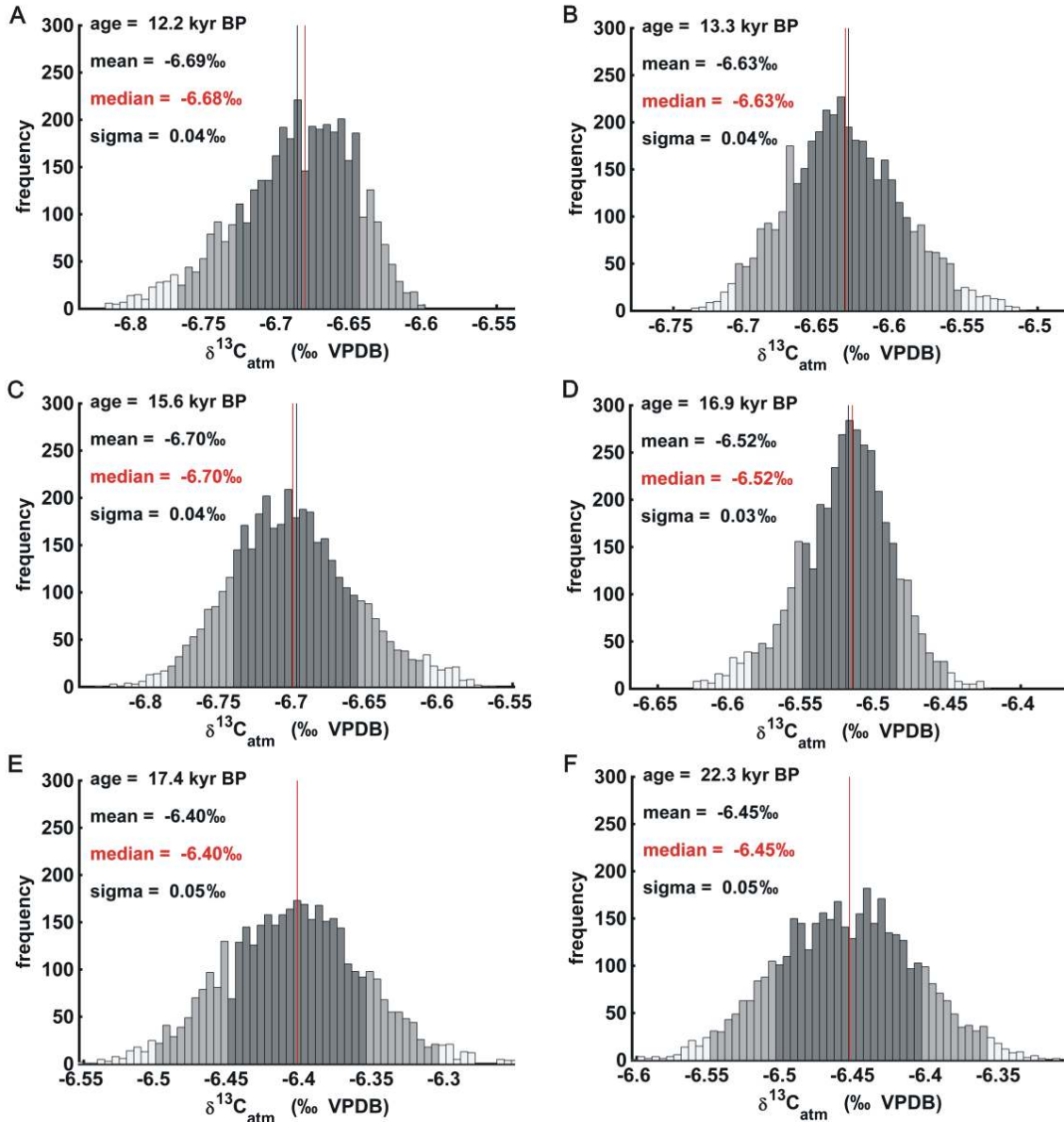
Fig. S5

Frequency distributions of the Monte Carlo splines at selected points in time: Histograms showing the distributions of the 4000 splines at selected points of our $\delta^{13}C_{atm}$ time series (positions marked in Fig. S4 with brown Latin letters). Bars in dark gray mark the 1σ interval, light gray the 2σ interval, and white bars are outside the 2σ interval. The black (red) vertical line marks the mean (median) of the distribution. Note that some distributions are not Gaussian but have a broader shape; therefore, mean and standard deviation do not entirely describe the frequency distributions.
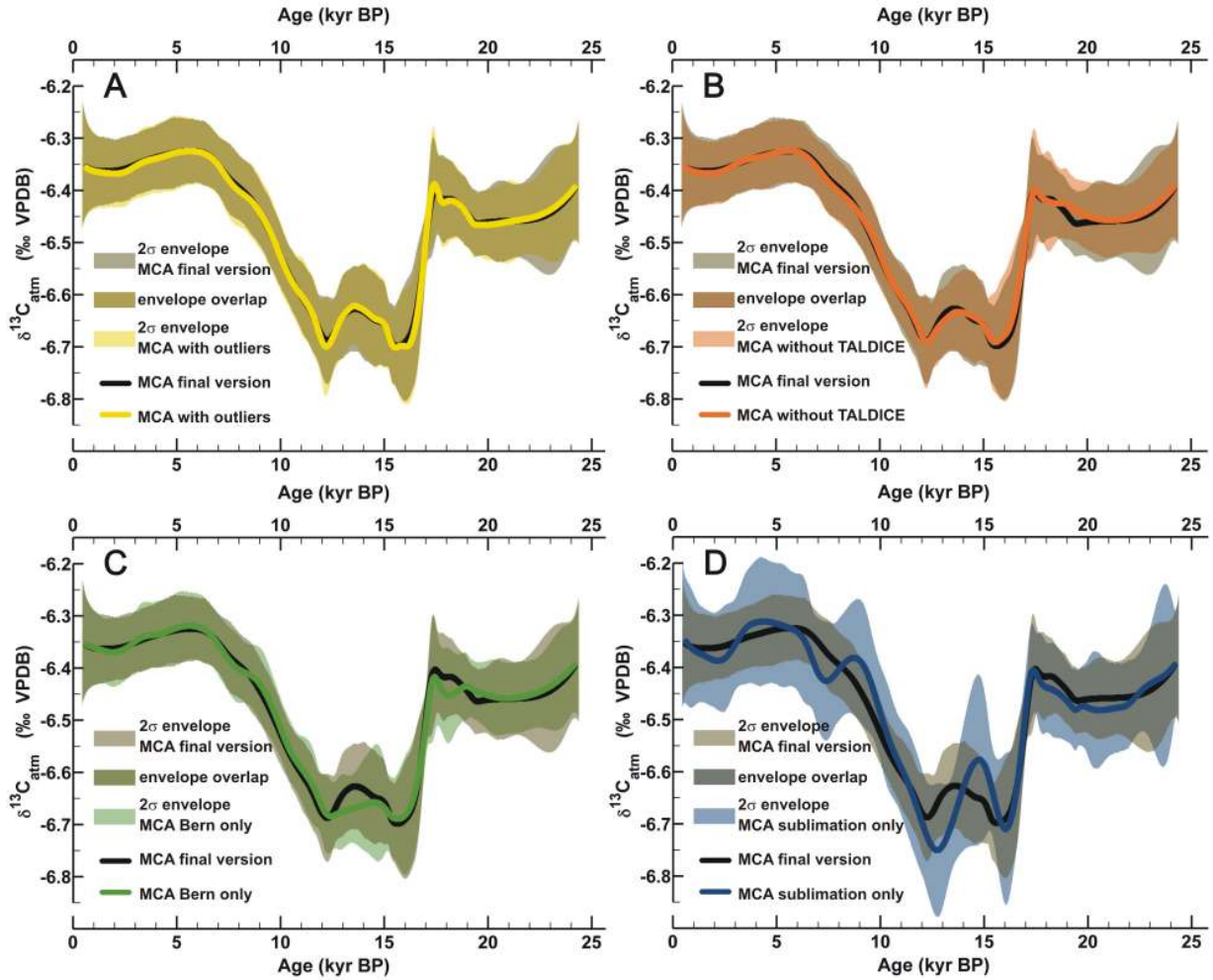
Fig. S6

Comparison of Monte Carlo Averages for different data sets included. Each panel shows the final MCA in black, i.e. the MCA which is used in the main figures Fig. 1 and Fig. 2 of the paper and on which the interpretations are based. The individual MCAs in the sub-panels **A-D** are plotted in colors. The 2σ envelope of the final MCA is in gray and the 2σ envelopes of sub-panels **A-D** are colored and overlapping 2σ envelopes are in the respective mixed tones. **A** All three data sets but with the five outliers detected in the bootstrap routine included. **B** TALDICE samples excluded **C** Only Bern cracker and Bern sublimation data (i.e. Grenoble ball mill data excluded) **D** Bern sublimation data only. While the calculated MCA is insensitive to the outliers and the TALDICE samples, removing the Grenoble ball mill data and Bern cracker data has an effect on the MCA. In case of removing the Grenoble data, the calculated MCA deviates somewhat from the final MCA between 12 and 14 kyr, where there is the largest disagreement among the three data set. However, the overall shape is retained. When only the sublimation data is used, the MCA becomes unstable and pinned at individual data points, since the resolution is insufficient for the applied cut-off period of 375 years. All exclusion experiments show that the respective 2σ envelopes overlap and thus record the same robust $\delta^{13}C_{atm}$ atmospheric features seen in the final MCA.
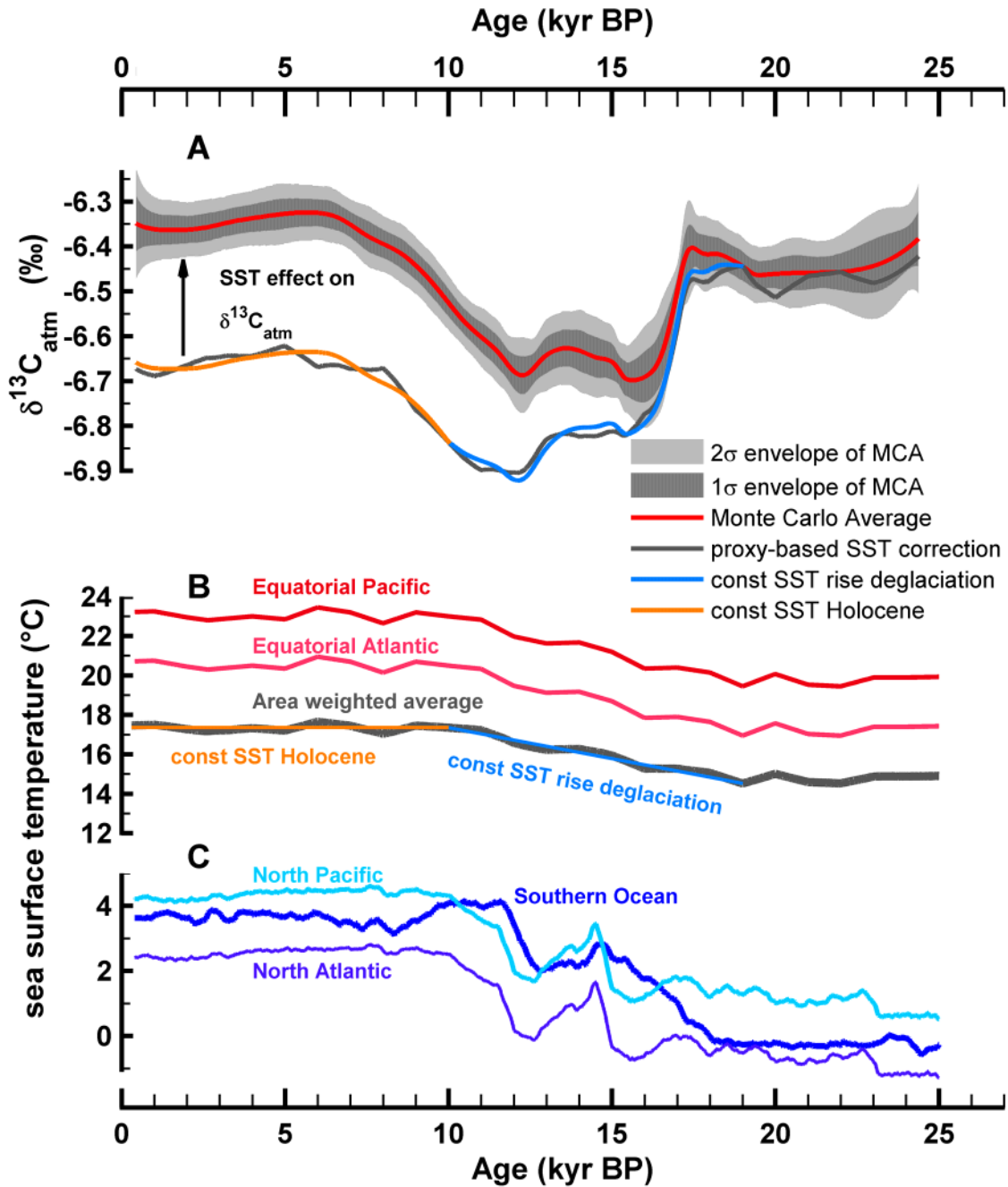
Fig. S7

SST correction of the $\delta^{13}C_{atm}$ MCA evolution. A proxy-based SST reconstruction is compared with a linear temperature increase during the deglaciation. **(A)** Evolution of $\delta^{13}C_{atm}$ (red line) and proxy-based SST corrections (gray line) compared with a linear rise of 2.8 K between 19 kyr and 10 kyr (blue line) followed by constant SST during the Holocene (orange line). **(B)** SST evolution of the equatorial boxes (red lines) and the area-weighted average of all five surface boxes (gray), the latter being used for the proxy based SST correction above, **(C)** SST evolution of the three high latitude surface boxes (blue lines).

15

Table S1.

Selected points of the Monte Carlo Average and their respective mean, median, and 1σ standard deviation as used to calculate the time intervals shown in Tab. S2.

interval boundary	mean $\delta^{13}C_{atm}$	median $\delta^{13}C_{atm}$	1σ
(kyr BP)	(‰)	(‰)	(‰)
5.7	-6.32	-6.33	±0.03
12.2	-6.69	-6.68	±0.04
13.3	-6.63	-6.63	±0.04
15.4	-6.70	-6.70	±0.04
16.0	-6.69	-6.69	±0.06
17.4	-6.40	-6.40	±0.05
19.3	-6.46	-6.46	±0.03
24.0	-6.40	-6.40	±0.05

Table S2.

Time intervals listing the trends in mean $\delta^{13}C_{atm}$ and median $\delta^{13}C_{atm}$ between two interval boundaries as listed in Tab. S1 and marked in Fig. S4. As a conservative estimate of the confidence of these differences, the last column lists the sum of both 1σ standard deviations of $\delta^{13}C_{atm}$ at the interval boundaries. Note that interval 1, 2, 3, 5 and 7 represent the differences between local minima and maxima positions on the MCA. In contrast, intervals 4 and 7 were selected to represent relatively flat plateaus. Intervals 1 and 5 are indicated in bold to indicate that most of the $\delta^{13}C_{atm}$ variability is concentrated in these two intervals.

interval	interval boundaries	Δ mean $\delta^{13}C_{atm}$	Δ median $\delta^{13}C_{atm}$	Σ 1σ
#	(kyr BP)	(‰)	(‰)	(‰)
1	**12.2 - 5.7**	**0.37 ↑**	**0.35 ↑**	**±0.07**
2	13.3 - 12.2	0.06 ↓	0.05 ↓	±0.08
3	15.4 - 13.3	0.07 ↑	0.07 ↑	±0.08
4	16.0 - 15.4	0.01 ↓	0.01 ↓	±0.10
5	**17.4 - 16.0**	**0.29 ↓**	**0.29 ↓**	**±0.11**
6	19.3 - 17.4	0.06 ↑	0.06 ↑	±0.08
7	24.0 - 19.3	0.06 ↓	0.06 ↓	±0.08

References:

1. D. Lüthi *et al.*, High-resolution carbon dioxide concentration record 650,000-800,000 years before present. Nature **453**, 379 (2008). doi:10.1038/nature06949

2. H. Fischer *et al.*, The role of Southern Ocean processes in orbital and millennial CO_2 variations - A synthesis. Quat. Sci. Rev. **29**, 193 (2010). doi:10.1016/j.quascirev.2009.06.007

3. E. Monnin *et al.*, Atmospheric CO_2 concentration over the last termination. Science **291**, 112 (2001).

4. P. Köhler, H. Fischer, G. Munhoven, R. E. Zeebe, Quantitative interpretation of atmospheric carbon records over the last glacial termination. Global Biogeochem. Cycles **19**, GB4020 (2005). doi:10.1029/2004GB002345

5. D. M. Sigman, M. P. Hain, G. H. Haug, The polar ocean and glacial cycles in atmospheric CO_2 concentration. Nature **466**, 47 (2010). doi: 10.1038/nature09149

6. J. Elsig *et al.*, Stable isotope constraints on Holocene carbon cycle changes from an Antarctic ice core. Nature **461**, 507 (2009). doi:10.1038/nature08393

7. H. J. Smith, H. Fischer, M. Wahlen, D. Mastroianni, B. Deck, Dual modes of the carbon cycle since the Last Glacial Maximum. Nature **400**, 248 (1999). doi: 10.1038/22291

8. M. Leuenberger, U. Siegenthaler, C. C. Langway, Carbon isotope composition of atmospheric CO_2 during the last ice age from an Antarctic ice core. Nature **357**, 488 (1992).

9. A. Lourantou *et al.*, Constraint of the CO_2 rise by new atmospheric carbon isotopic measurements during the last deglaciation. Global Biogeochem. Cycles **24**, GB2015 (2010). doi:10.1029/2009GB003545

10. J. Schmitt, R. Schneider, H. Fischer, A sublimation technique for high-precision measurements of $\delta^{13}CO_2$ and mixing ratios of CO_2 and N_2O from air trapped in ice cores. Atmos. Meas. Tech. **4**, 1445 (2011). doi:10.5194/amt-4-1445-2011

11. P. Köhler, H. Fischer, J. Schmitt, Atmospheric $\delta^{13}CO_2$ and its relation to pCO_2 and deep ocean $\delta^{13}C$ during the late Pleistocene. Paleoceanography **25**, PA1213 (2010). doi:10.1029/2008PA001703

12. J. Zhang, P. D. Quay, D. O. Wilbur, Carbon isotope fractionation during gas-water exchange and dissolution of CO_2. Geochim Cosmochim Ac **59**, 107 (1995).

13. K. I. C. Oliver *et al.*, A synthesis of marine sediment core $\delta^{13}C$ data over the last 150 000 years. Clim. Past **6**, 645 (2010). doi:10.5194/cp-6-645-2010

14. P. J. Reimer *et al.*, Intcal09 and Marine09 Radiocarbon Age Calibration Curves, 0-50,000 Years Cal BP. Radiocarbon **51**, 1111 (2009).

15. J. Southon, A. L. Noronha, H. Cheng, R. L. Edwards, Y. Wang, A high-resolution record of atmospheric ^{14}C based on Hulu Cave speleothem H82. Quat. Sci. Rev. **33**, 32 (2012). doi: 10.1016/j.quascirev.2011.11.022

16. P. Köhler, R. Muscheler, H. Fischer, A model-based interpretation of low-frequency changes in the carbon cycle during the last 120,000 years and its implications for the reconstruction of atmospheric $\Delta^{14}C$. Geochem. Geophys. Geosyst. **7**, Q11N06 (2006). doi: 10.1029/2005GC001228

17. C. Laj, C. Kissel, J. Beer, in *Timescales of the Paleomagnetic Field*. (American Geophysical Union, 2004), vol. 145, pp. 255-265.

18. R. Muscheler, R. Beer, P. W. Kubik, H. A. Synal, Geomagnetic field intensity during the last 60,000 years based on ^{10}Be and ^{36}Cl from the Summit ice cores and ^{14}C. Quat. Sci. Rev. **24**, 1849 (2005). doi:10.1016/j.quascirev.2005.01.012

19. W. Broecker, S. Barker, A 190‰ drop in atmosphere's $\Delta^{14}C$ during the "Mystery Interval" (17.5 to 14.5 kyr). Earth Planet. Sci. Lett. **256**, 90 (2007). doi: 10.1016/j.epsl.2007.01.015

20. R. F. Anderson *et al.*, Wind-Driven Upwelling in the Southern Ocean and the Deglacial Rise in Atmospheric CO_2. Science **323**, 1443 (2009).

21. P. Ciais *et al.*, Large inert carbon pool in the terrestrial biosphere during the Last Glacial Maximum. Nat. Geosci **5**, 74 (2012). doi: 10.1038/NGEO1324

22. J. M. Yu *et al.*, Loss of Carbon from the Deep Sea Since the Last Glacial Maximum. Science **330**, 1084 (2010).

23. D. C. Lund, A. C. Mix, J. Southon, Increased ventilation age of the deep northeast Pacific Ocean during the last deglaciation. Nat. Geosci. **4**, 771 (2011). doi:10.1038/ngeo1272

24. L. Stott, J. Southon, A. Timmermann, A. Koutavas, Radiocarbon age anomaly at intermediate water depth in the Pacific Ocean during the last deglaciation. Paleoceanography **24**, PA2223 (2009). doi:10.1029/2008PA001690

25. W. Broecker, E. Clark, Search for a glacial-age ^{14}C-depleted ocean reservoir. Geophys. Res. Lett. **37**, L13606 (2010). doi:10.1029/2010GL043969

26.   A. Burke, L. F. Robinson, The Southern Ocean's role in carbon exchange during the last deglaciation. Science **335**, 557 (2012). doi: 10.1126/science.1208163

27.   E. Bard, F. Rostek, J. L. Turon, S. Gendreau, Hydrological impact of Heinrich events in the subtropical northeast Atlantic. Science **289**, 1321 (2000).

28.   T. Tschumi, F. Joos, M. Gehlen, C. Heinze, Deep ocean ventilation, carbon isotopes, marine sedimentation and the deglacial CO_2 rise. Clim. Past **7**, 771 (2011). doi: 10.5194/cp-7-771-2011

29.   R. Zech, Y. Huang, M. Zech, R. Tarozo, W. Zech, High carbon sequestration in Siberian permafrost loess-paleosols during glacials. Clim. Past **7**, 501 (2011). doi: 10.5194/cp-7-501-2011

30.   N. Zeng, Quasi-100 ky glacial-interglacial cycles triggered by subglacial burial carbon release. Clim. Past **3**, 135 (2007).

31.   D. A. Hodell, C. D. Charles, F. J. Sierro, Late Pleistocene evolution of the ocean's carbonate system. Earth Planet. Sci. Lett. **192**, 109 (2001). doi: 10.1016/S0012-821X(01)00430-7

32.   B. Lemieux-Dudon *et al.*, Consistent dating for Antarctic and Greenland ice cores. Quat. Sci. Rev. **29**, 8 (2010). doi: 10.1016/j.quascirev.2009.11.010

33.   North Greenland Ice Core Project members, High-resolution record of Northern Hemisphere climate extending into the last interglacial period. Nature **431**, 147 (2004). doi: 10.1038/nature02805

34.   EPICA Community Members, One-to-one coupling of glacial climate variability in Greenland and Antarctica. Nature **444**, 195 (2006). doi: 10.1038/nature05301

35.   B. Stenni *et al.*, An oceanic cold reversal during the last deglaciation. Science **293**, 2074 (2001). doi: 10.1126/science.1059702

36.   J. Elsig, Dissertation, University of Bern (2009).

37.   D. Lüthi *et al.*, CO_2 and O_2/N_2 variations in and just below the bubble-clathrate transformation zone of Antarctic ice cores. Earth Planet. Sci. Lett. **297**, 226 (2010). doi:10.1016/j.epsl.2010.06.023

38.   G. Dreyfus, Phd Thesis, Princeton University (2008).

39.   G. B. Dreyfus *et al.*, Firn processes and $\delta^{15}N$: potential for a gas-phase climate proxy. Quat. Sci. Rev. **29**, 28 (2009).

40.   R. J. Francey *et al.*, A 1000-year high precision record of $\delta^{13}C$ in atmospheric CO_2. Tellus **51B**, 170 (1999).

41.   R. Spahni *et al.*, The attenuation of fast atmospheric CH_4 variations recorded in polar ice cores. Geophys. Res. Lett. **30**, 25 (2003).

42.   D. Buiron *et al.*, TALDICE-1 age scale of the Talos Dome deep ice core, East Antarctica. Clim. Past **7**, 1 (2011).

43.   I. G. Enting, On the Use of Smoothing Splines to Filter CO_2 Data. J. Geophys. Res.-Atmos. **92**, 10977 (1987). doi: 10.1029/JD092iD09p10977

44.   J. Schwander, B. Stauffer, A. Sigg, Air mixing in firn and the age of the air at pore close-off. Annals of Glaciology **10**, 141 (1988).

45.   A. Indermühle *et al.*, Holocene carbon-cycle dynamics based on CO_2 trapped in ice at Taylor Dome, Antarctica. Nature **398**, 121 (1999).

46.   R. E. Zeebe, D. A. Wolf-Gladrow, *CO_2 in seawater: equilibrium, kinetics, isotopes*, Elsevier Oceanography series (2005), pp. 65.

47.   P. M. Grootes, M. Stuiver, Oxygen 18/16 variability in Greenland snow and ice with 10^3- to 10^5 -year time resolution. J. Geophys. Res.-Oceans **102**, 26455 (1997).

48.   J. Jouzel *et al.*, Orbital and millennial Antarctic climate variability over the past 800,000 years. Science **317**, 793 (2007). doi: 10.1126/science.1141038

49.   K. Visser, R. Thunell, L. Stott, Magnitude and timing of temperature change in the Indo-Pacific warm pool during deglaciation. Nature **421**, 152 (2003).